CHAPTER 4

TRIBOLOGICAL BEHAVIOR OF COPPER BASED HYBRID COMPOSITES CONTAINING Al_2O_3, MoS_2 AND *h*-BN

This chapter describes the results on the X- ray diffraction and microstructural examination of Copper based hybrid composites containing either a hard phase or a combination of hard as well as solid lubricating phases (es) i.e. Cu-Fe- Al_2O_3, Cu-Fe-Al_2O_3-MoS_2 and Cu-Fe-Al_2O_3-MoS_2-*h*-BN synthesized via spark plasma sintering. The results on density and hardness of the composites are also presented along with the results on dry sliding friction and wear behavior of the composites. In the end results have been discussed to develop an understanding of the effect of addition of a combination of a hard and soft phase or a combination of solid lubricants in governing the tribological performance of developed composites.

4.1 RESULTS

4.1.1 CHARACTERIZATION OF COMPOSITES

Figure 4.1 shows the XRD patterns of pure Cu (PC) and composites Cu-Fe-Al_2O_3 (CA), Cu-Fe-Al_2O_3-MoS_2 (CAM) and Cu-Fe-Al_2O_3-MoS_2-*h*-BN (CAMB). The peaks corresponding to characteristic features of copper (JCPDS card no. 85-1326) are found to be present in both pure Cu and Cu-based hybrid composites. One may observe the peak at 2θ of 36.5° corresponding to (104) plane of Al_2O_3 in composite CA and the peak corresponding to (101) plane of MoS_2 at 2θ of 13.7° in their respective XRD

patterns. XRD features of CAMB composite exhibit the presence of peaks at 2θ of 13.7°, 26.6° corresponding to (101) plane MoS_2 and (002) plane of *h*-BN (JCPDS card no. 85-1068), respectively, along with the peak of Al_2O_3. No extra peak has been observed in any of the composites except those of the constituent components, indicating that all the constituent components are present in the composite in their original form.

Figures 4.2 (a through c) present SEM micrographs showing microstructure of composites Cu-Fe-Al_2O_3 (CA), Cu-Fe-Al_2O_3-MoS_2 (CAM) and Cu-Fe-Al_2O_3-MoS_2-*h*-BN (CAMB), respectively, under scattered as well as back-scattered modes. All the micrographs shown in Fig. 4.2 are in scattered mode, while the images shown in the inset correspond to backscattered mode. The microstructure of composite CA depicted in Fig. 4.2 (a) shows the dispersion of alumina particles along with presence pores/voids at the grain boundaries as evident from the inset. The micrograph corresponding to composite CAM, shown in Fig. 4.2 (b) reveals several light-shaded regions at grain boundaries in the back-scattered mode image, which signify the good dispersion of reinforcing materials Al_2O_3 and MoS_2 (marked by arrows) in the CAM composite and the same is supported by scattered mode image. Moreover, the CAM appears to have a lesser number of voids compared to the CA composite. The microstructure of composite CAMB given in Fig. 4.2 (c) shows the presence of *h*-BN nanoparticles, MoS_2 and Al_2O_3 as indicated by arrows along with some agglomerates at grain boundaries in scattered and backscattered mode (inset) of microscopic images of CAMB composite. The agglomeration of *h*-BN is expected to result in an increase in voids at grain boundaries in the CAMB composite.

Figure 4.3 depicts the micrographs along with corresponding area elemental distribution of Cu-based composites. The abundance of Al and O at the grain boundary regions of CA composite seen in Fig. 4.3 suggest the agglomeration of alumina on grain

boundaries which is also observed in Fig. 4.2 (a). Elemental mapping corresponding to CAM composite shown in Fig. 4.3 (b) reflects a thorough distribution of Al, O, Mo, and S in matrix of Cu which also confirms the presence of the alumina and MoS_2 in CAM composite as revealed in Fig. 4.2 (b). The presence of Al, O, Mo, S, B, and N in the elemental mapping corresponding to CAMB given in Fig. 4.3 (c) shows that the composite contains *h*-BN, alumina and MoS_2 as observed in Fig. 4.2 (c) also.

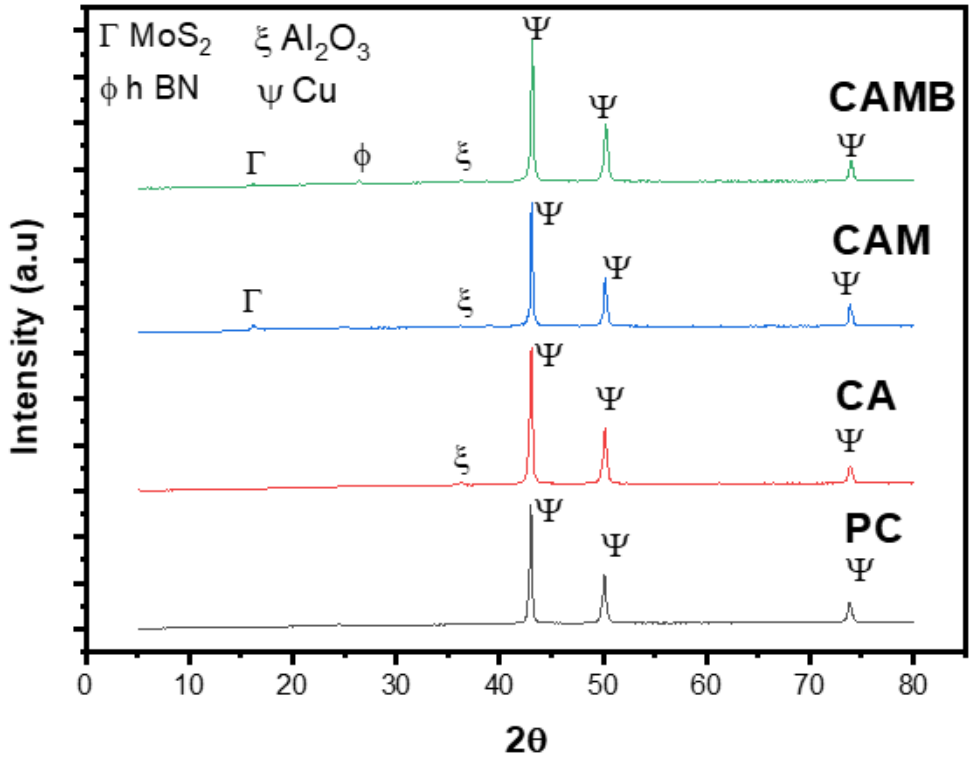

Fig. 4.1 XRD patterns of pure copper and composites fabricated by Spark plasma sintering.

Table 4.1 shows the density and hardness of pure Cu and Cu-based hybrid composites, which includes both theoretical and calculated densities. The CAM composite has been found to possess maximum relative density among all the materials investigated in the present study, which is followed by the density of composite CA, pure copper and CAMB. The hardness has been found to increase with addition of Fe and Al_2O_3 (CA) and Fe, Al_2O_3 and MoS_2 (CAM) in Cu matrix as evident from Table 4.1.

However, a reduction in hardness is observed with addition of *h*-BN apart from Fe, Al_2O_3 and MoS_2 (CAMB).

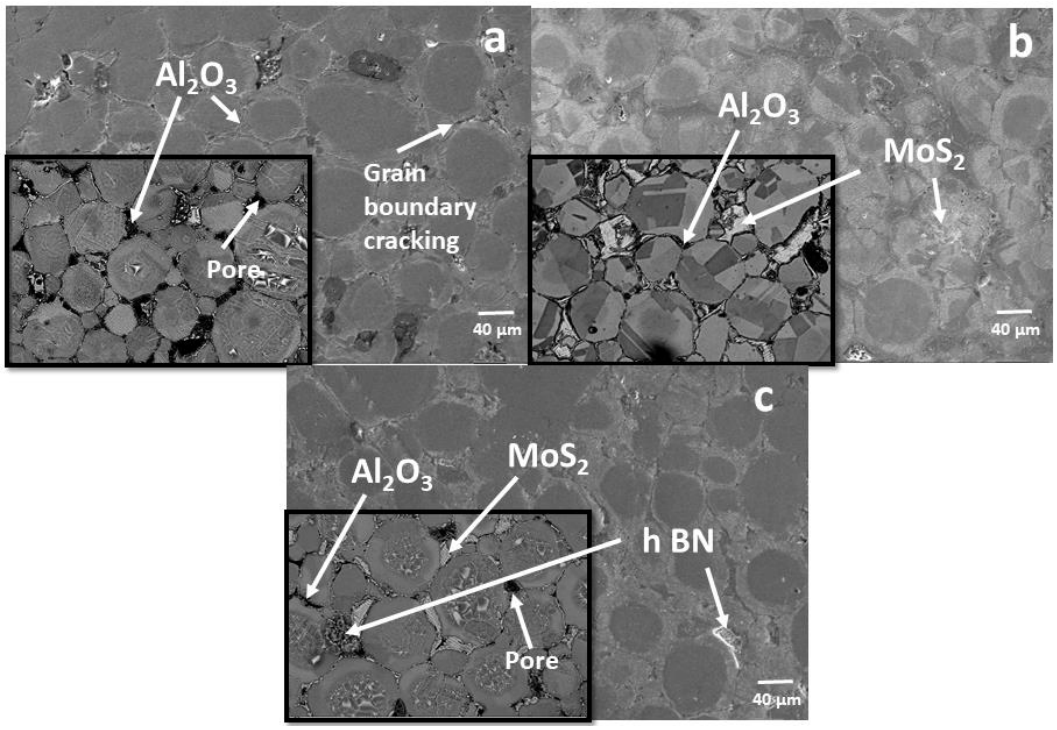

Fig. 4.2 Micrographs of (a) CA, (b) CAM, and (c) CAMB composites captured by SEM under the scattered mode. Inset images correspond to the back-scattered mode of respective composites.

Table 4.1 Density and hardness of Cu-based hybrid composites

Sample	Theoretical Density, g/cm^3	Actual Density, g/cm^3	Relative Density, %	Hardness $HV_{0.3}$
Pure Cu (C)	8.959	8.203	91.5	52.5
Cu-Fe-Al_2O_3 (CA)	8.715	8.277	94.9	97.2
Cu-Fe-Al_2O_3-MoS_2 (CAM)	8.326	8.176	98.1	101.3
Cu-Fe-Al_2O_3-MoS_2-*h*-BN (CAMB)	8.178	7.306	89.3	77.56

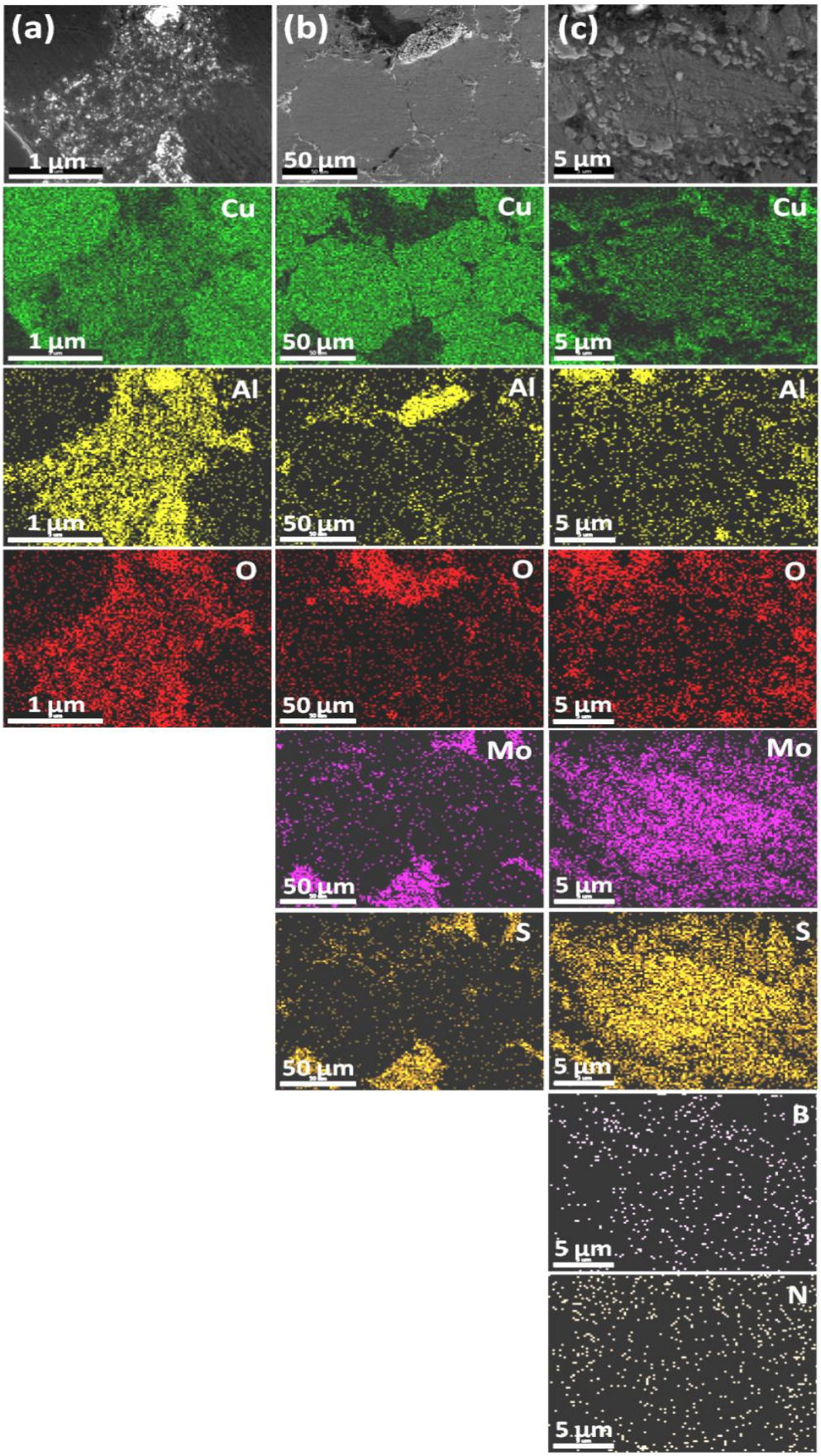

Fig. 4.3 Scanning electron micrographs along with corresponding area elemental distribution of (a) CA, (b) CAM and (c) CAMB composites.

4.1.2 FRICTION AND WEAR BEHAVIOR

Figure 4.4 shows the variation of friction coefficient with a number of cyclic contacts at the load of 8 N load and sliding speed of 0.5 $m.s^{-1}$ for pure Cu and Cu-based hybrid composites. The pure Cu and CAMB composite exhibits stable friction profiles, whereas both CA and CAM composites show significant variation in their friction profiles with the function of cyclic contacts. The CAM composite exhibits a low coefficient of friction (< 0.2) during initial 1200 cycles followed by a sudden increase in the coefficient of friction, before reaching a stabilized value ~ 0.6. The pure Cu has been observed to exhibit the lowest coefficient of friction throughout the test. The CA composite has been found to show a relatively higher friction with larger amplitude of fluctuations throughout the test, whereas CAMB composite has shown a high coefficient of friction in the same range as that of CA composite but with a stabilized friction profile.

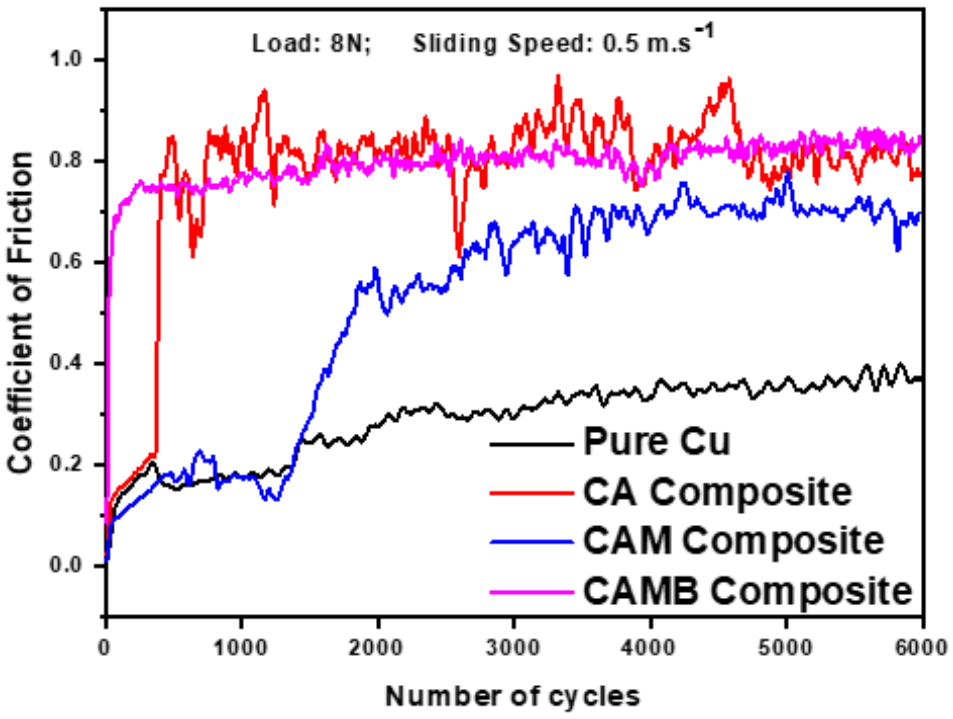

Fig. 4.4 Variation of coefficient of friction for pure Cu and Cu-based hybrid composites at a load of 8N load and sliding speed of 0.5 $m.s^{-1}$.

Figure 4.5 shows the variation of average coefficient of friction for pure Cu and Cu-based hybrid composites with load and composition, which has been obtained for each measurement when the friction curve stabilizes and becomes steady. The average coefficient of friction has been found to increase with increase in load from 2 to 4 N for all the materials as seen from Fig. 4.5 (a). The pure Cu shows a reduction in coefficient friction as the applied load increases from 4 to 8 N, whereas, the coefficient of friction is found to increase beyond 4 N load for composite CA. The composite containing Al_2O_3 and MoS_2 i.e. CAM exhibits no significant changes in coefficient of friction from 4 to 8N, whereas CAMB composite shows a slight decrease in the average coefficient of friction on increasing the load beyond 4N. The variation of average coefficient of friction as a function of composition illustrated in Fig. 4.5 (b) reveals that composite CAM has the minimum coefficient of friction at all loads except at 8N. Among all the materials tested, pure copper has shown the lowest average coefficient of friction at 8N loading condition as evident from Fig.4.5 (b). One may also observe that composites CA and CAMB have relatively lower coefficient of friction than pure Cu at all the loads except 8 N, however, these composites have a relatively higher coefficient of friction than CAM at all the loads.

The variation in wear rate for pure Cu and Cu-based hybrid composites as a function of load is shown in Fig. 4.6 (a). The wear rate for all the specimens is found to increase with load, when the applied load is raised from 2 to 4 N, as observed in Fig. 4.6 (a). However, the increase is relatively less in CAM in comparison to others. Interestingly, the wear rate of pure Cu, CAM, and CAMB specimens has been observed to decrease gradually as the load is increased from 4 to 8 N, in contrast to composite CA which has exhibited an increasing trend of wear with increasing load beyond 4 N. However, composite CAM has shown the lowest wear rate under all the loads except 2 N and among

all the materials investigated in the present study as evident from Fig. 4.6 (a). The variation of wear rate with respect to composition for pure Cu and the synthesized composites illustrated in Fig. 4.6 (b) indicates that composite CAM has the minimum wear rate amongst all materials studied in the present work.

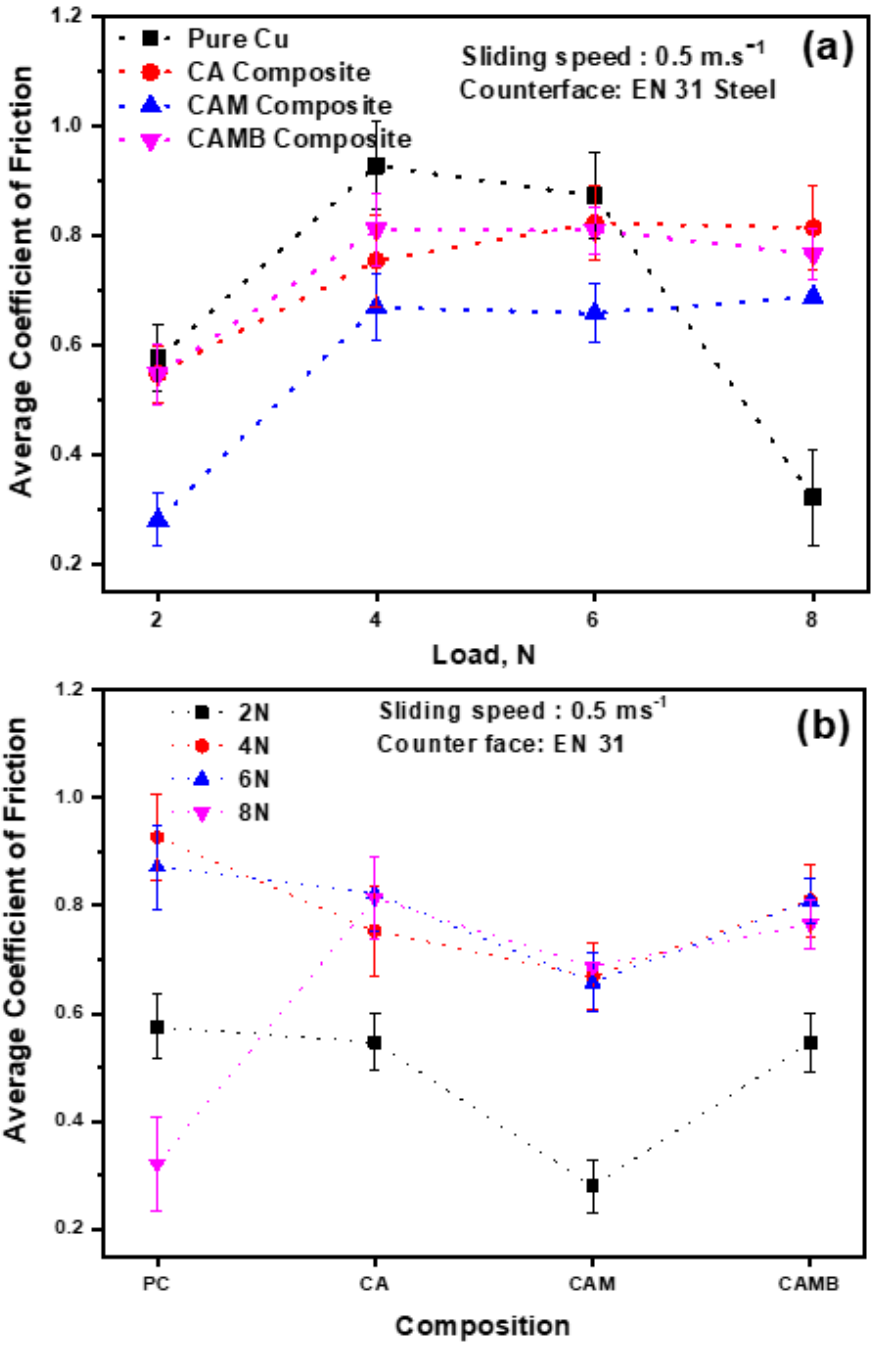

Fig. 4.5 Variation of the average coefficient of friction for pure Cu and Cu-based hybrid composites as functions of (a) load and (b) composition.

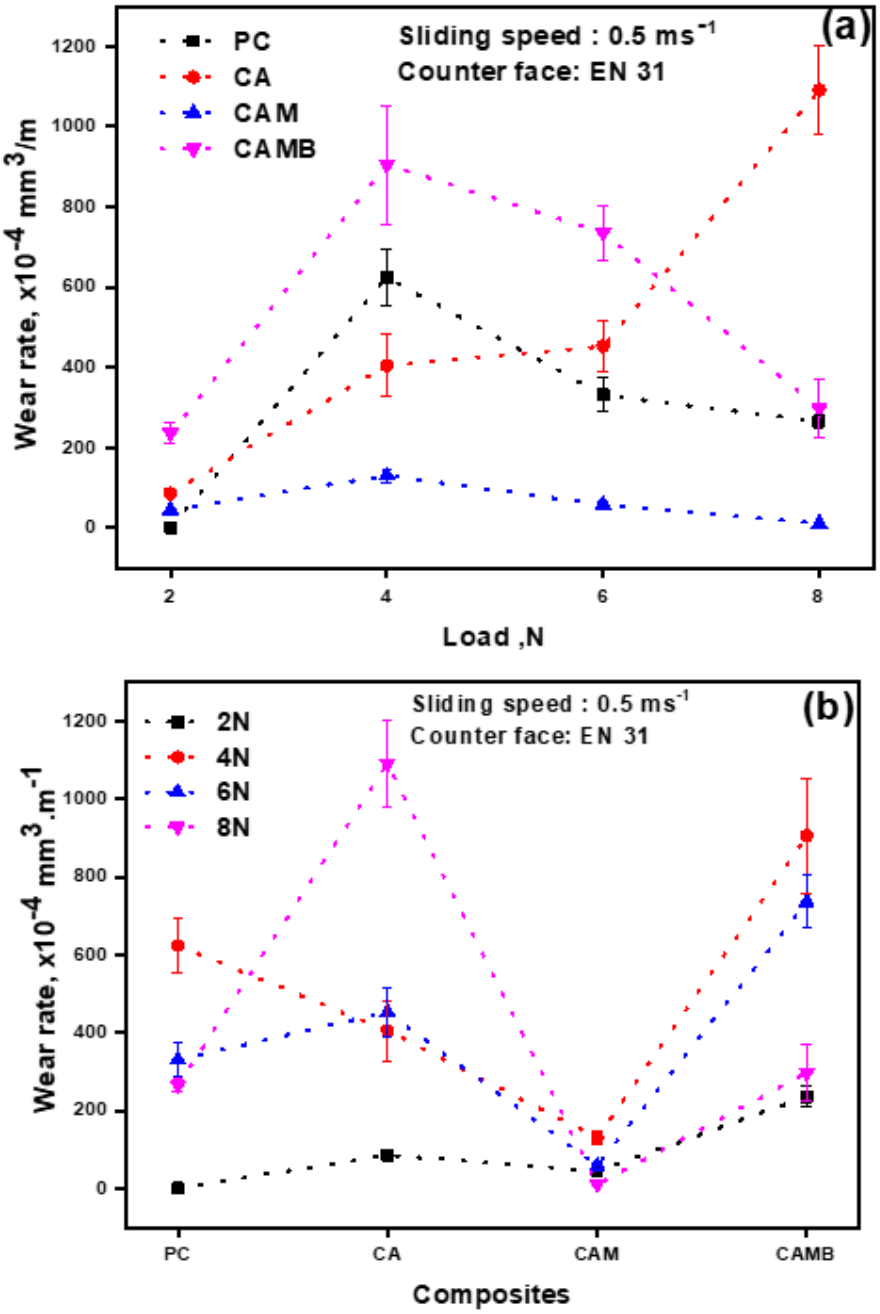

Fig. 4.6 Variation of wear rate for PC and composites with (a) normal load and (b) composition.

Figure 4.7 shows the SEM micrographs of the worn surfaces of pure Cu and composites CA, CAM, CAMB slid against the EN 31 steel ball at a load of 2 N and speed of 0.5 $m.s^{-1}$. The worn surface of pure Copper shown in Fig. 4.7 (a) exhibits minor adhesion, whereas delamination is observed to be a plausible wear event for CA, as shown in Fig. 4.7 (b), moreover, bright patches on the worn surface of CA also suggest the

occurrence of oxidation. The worn tracks of CAM and CAMB composites along with respective EDS analyses (both as at. % and wt. %) are shown in Figs. 4.7 (c) and (d), respectively. One may observe the presence of a tribo-layer rich in Cu, Fe and Mo on the worn surface of both CAM and CAMB as indicated by the elemental analysis. In addition, the worn track of CAMB composite also exhibits bright patches, suggesting the presence of *h*-BN on the worn surface.

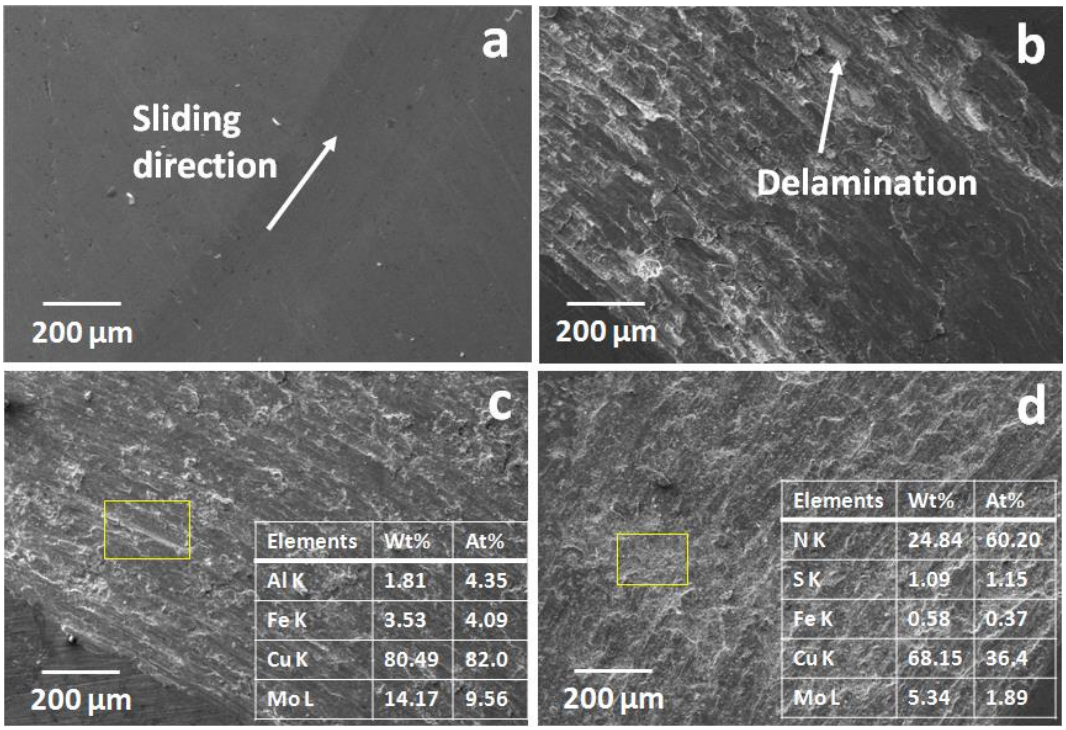

Elements	Wt%	At%
Al K	1.81	4.35
Fe K	3.53	4.09
Cu K	80.49	82.0
Mo L	14.17	9.56

Elements	Wt%	At%
N K	24.84	60.20
S K	1.09	1.15
Fe K	0.58	0.37
Cu K	68.15	36.4
Mo L	5.34	1.89

Fig. 4.7 SEM micrographs of worn surfaces of (a) pure Cu and (b-d) Cu-based hybrid composites CA, CAM, and CAMB, respectively. Atomic % of elements on the worn surfaces of CAM and CAMB composites are shown based on the EDX measurements. The EN 31 steel ball was used as counterface. Load: 2 N, sliding speed: 0.5 $m.s^{-1}$.

Figure 4.8 shows the SEM micrographs of the worn surfaces for pure Cu and Cu-based composite after sliding under a load of 4 N and a sliding speed of 0.5 m. s^{-1}. The worn track on pure Cu exhibits, the characteristics features of severe abrasive wear signified by deep scoring and ploughing marks along the direction of sliding as indicated by white arrows in Fig. 4.8 (a). The worn surface of composite CA given in Fig. 4.8 (b)

shows signs of oxidation and delamination, whereas worn surface of composite CAM presented in Fig. 4.8 (c) reveals the formation of a compacted layer along with delamination at a few locations. The worn surface of composite CAMB shown in Fig. 4.8 (d) exhibits plastic deformation and the bright layer formation over the surface.

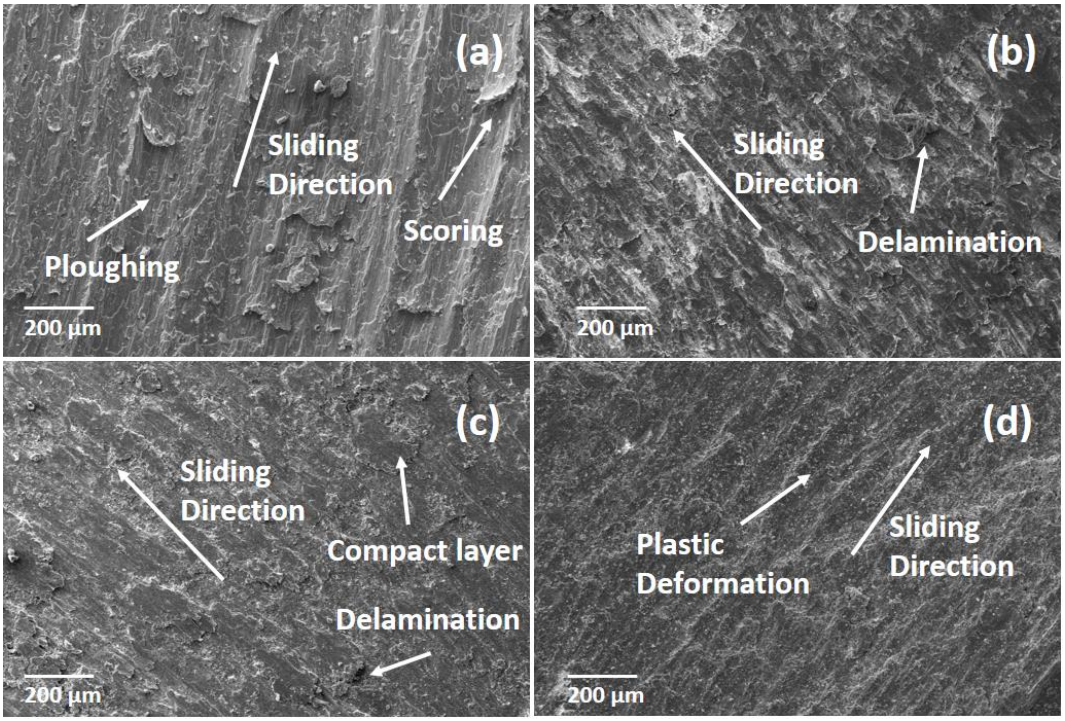

Fig. 4.8 SEM micrographs of worn surfaces of (a) pure Cu and (b-d) Cu-based hybrid composites CA, CAM, and CAMB, respectively. The EN 31 steel ball was used as counter face. Load: 4 N, sliding speed: 0.5 $m.s^{-1}$.

Figures 4.9 (a through d) show the SEM micrographs of the worn surfaces of pure Copper, CA, CAM and CAMB, respectively, after being slid at a load of 8 N under a sliding speed of 0.5 $m.s^{-1}$. The adhesive wear is believed to be a major wear mechanism in Fig. 4.9 (a) for pure Cu under the load of 8 N, while the worn track of CA composite is noted to be enriched with aggregates of loose wear debris, which could be associated with high oxidation of the material, as shown in Fig. 4.9 (b). A well compacted transfer layer along with some delamination features could be easily observed on the worn track of composite CAM shown in Fig. 4.9 (c). The micrograph of composite CAMB composite

shown in Fig. 4.9 (d) exhibits a mechanically mixed and loosely bound layer of wear debris smeared over the worn surface.

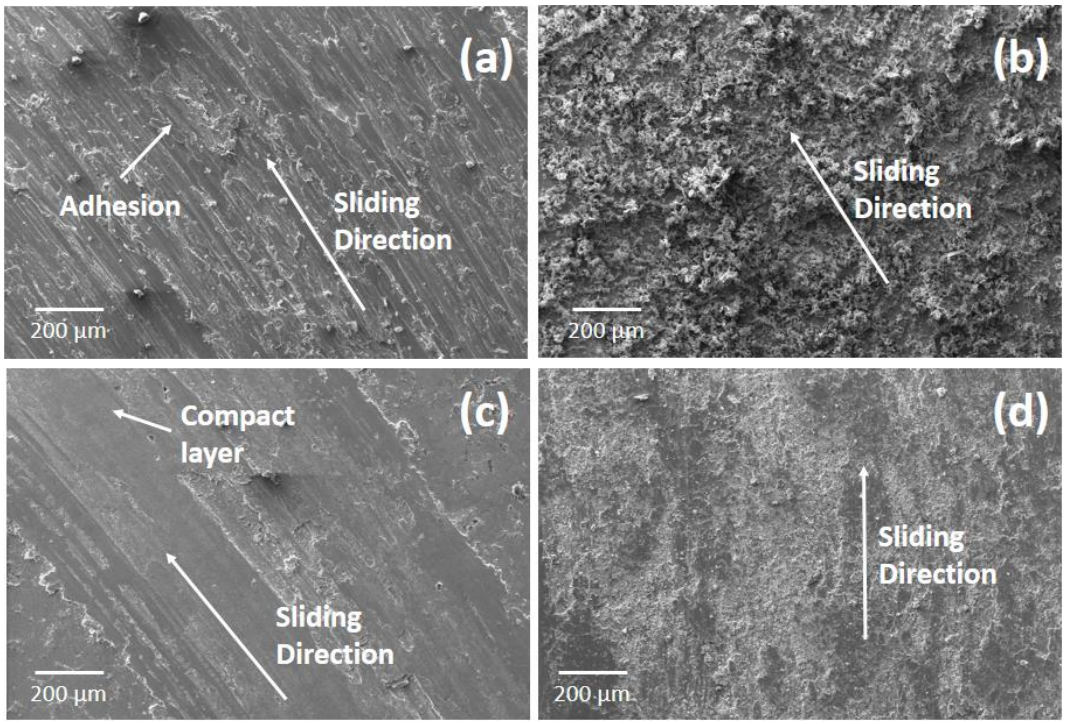

Fig. 4.9 SEM micrographs of worn surfaces of (a) pure Cu and (b-d) Cu-based hybrid composites CA, CAM, and CAMB, respectively. The EN 31 steel ball was used as counter face. Load: 8 N, sliding speed: 0.5 $m.s^{-1}$.

The XRD patterns of worn tracks of pure Cu as well as composites slid under a load of 8 N are depicted in Fig. 4.10. The characteristic features corresponding to copper (JCPDS card no. 85-1326) are found in both pure Cu and Cu-based hybrid composites. A lower concentration of reinforced materials in the Cu-based hybrid composites results in very weak signatures of these in XRD pattern, hence, their XRD peaks have been enlarged and the same are shown in respective insets of all composite specimens. The CA composite exhibits the peaks at 2θ of 36.5° corresponding to (104) plane of Al_2O_3 (JCPDS card no. 65-3288) and 2θ of 38.7° signifying the (111) plane of CuO (JCPDS card no. 89-5895) as seen from Fig. 4.10 (b). The worn track of CAM composite (Figure 4.10 c) shows the peaks at 2θ of 13.7° and 16.3° corresponding to (101) plane of MoS_2 and (101)

plane of Mo_2S_3, respectively, whereas, the worn track of CAMB composite exhibits XRD features at 2θ of 13.7°, 26.6° and 24.2° corresponding to (101) plane MoS_2, (002) plane of *h*-BN (JCPDS card no. 85-1068) and (101) plane of $B_{15}Mo_4$.

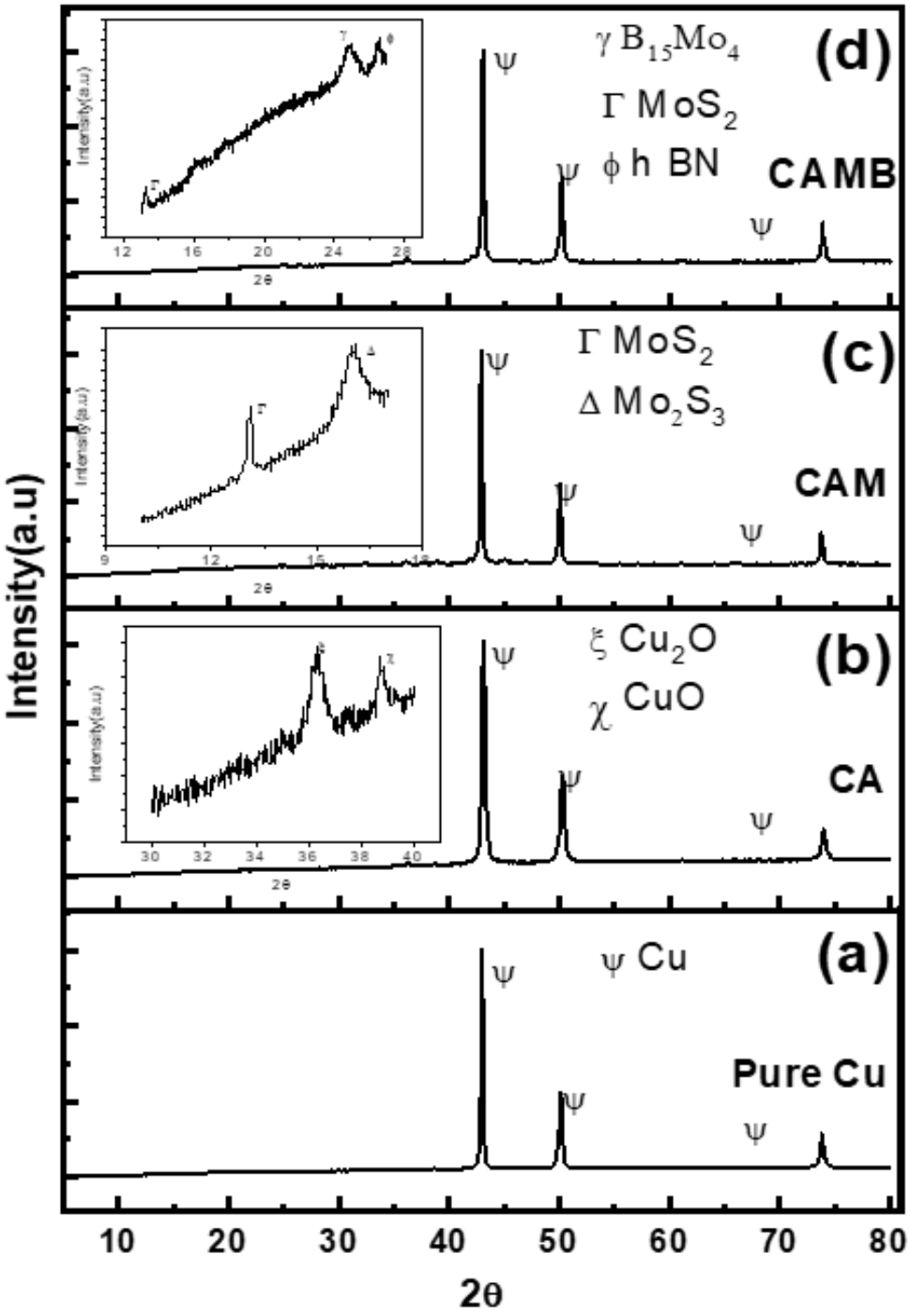

Fig. 4.10 XRD patterns of worn tracks developed on (a) pure Cu and (b-d) Cu-based hybrid composites CA, CAM, and CAMB, respectively under the load of 8 N.

Figure 4.11 shows SEM micrographs of the counterface EN 31 steel balls slid against the pure Cu and Cu-based hybrid composites under a load of 8 N. The worn surface micrograph of ball slid against pure Cu reveals the presence of some adhered material which might have been transferred from the Copper disc thus suggesting, the possibility of adhesion during the tribo-test as seen from Fig. 4.11 (a). One may observe the presence of a lump of material transferred from composite on the worn surface of the ball slid against composite CA as seen from Fig. 4.11 (b). The worn surface of counterface ball corresponding to composite CAM exhibits the formation of thin film, which can be seen from SEM micrograph presented in the Fig. 4.11 (c) whereas, a crescent shape bright feature along with some sliding marks could be seen on the worn surface of the ball corresponding to CAMB composite as evident in Fig. 4.11 (d).

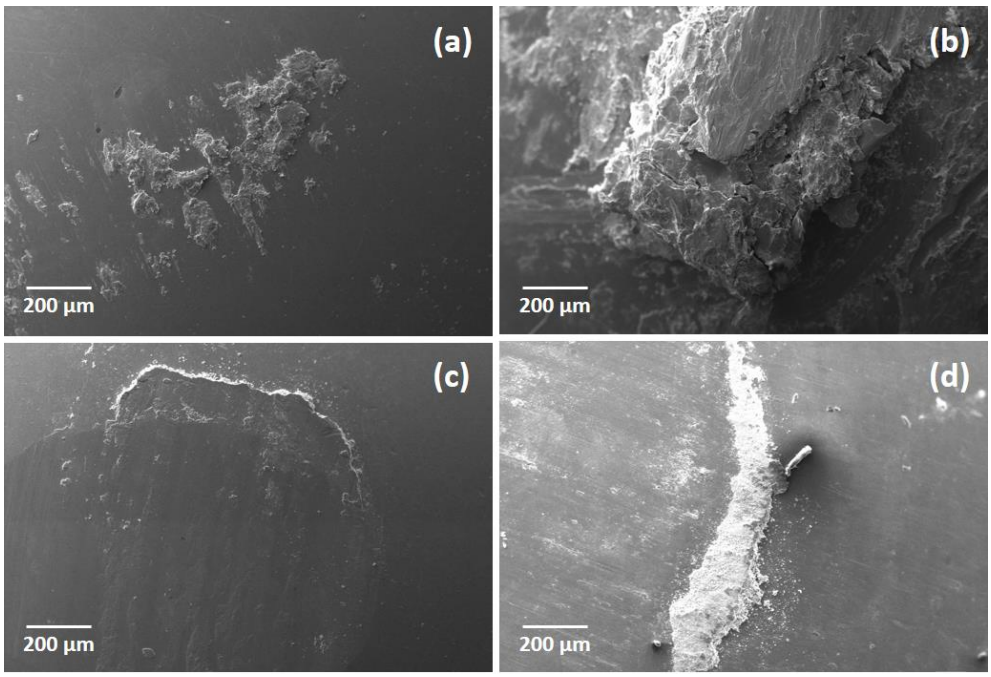

Fig. 4.11 SEM micrographs of the counter surface of EN 31 steel balls used for sliding against (a) pure Cu and (b-d) Cu-based hybrid composites CA, CAM, and CAMB, respectively. Load: 8 N

Figure 4.12 depicts SEM micrographs of the wear debris collected for CA and CAMB composites after the wear tests conducted at a load of 8 N. The wear debris

particles generated during wear testing of CAM composite has been very less in amount and hence, could not be examined. One may observe the presence of the particles with different sizes in the micrograph corresponding to composite CA given in Fig. 4.12 (a). The wear debris of CA composite reveals a flaky and scratchy appearance for bigger particles, whereas rough features could be observed for smaller debris particles. The wear debris particles generated during sliding of composite CAMB shown in Fig. 4.12 (b) are observed to be fine and equiaxed. Moreover, one may also observe the presence of very fine bright powder like debris in Fig. 4.12 (b). The size of wear particles corresponding to composite CA have been estimated to be at least ten times bigger than those corresponding to CAMB composite under identical sliding conditions.

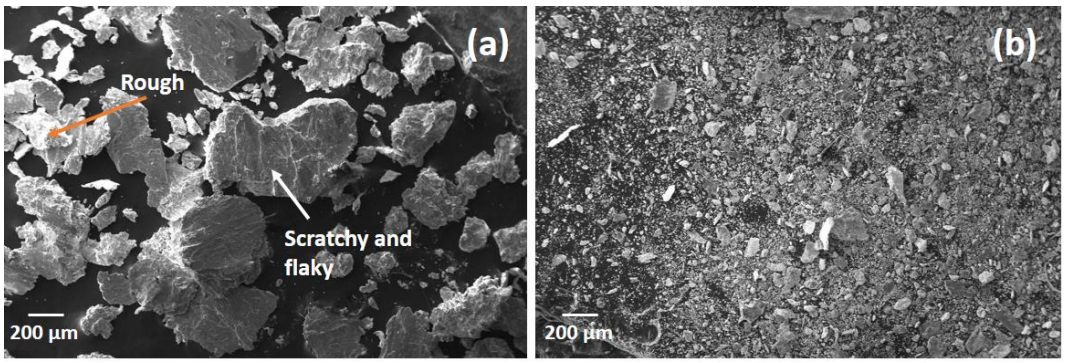

Fig. 4.12 SEM micrographs of wear debris collected from the (a) CA and (b) CAMB composites after the wear test at 8 N.

The microscopic analysis of subsurface is useful to probe the plastic deformation events that might have taken place during wear test. Hence, sub-surfaces of the specimens of pure Cu as well as composites, worn under a load of 8 N have been examined under Field Emission Scanning Electron Microscope (FESEM) and respective images are illustrated in Fig. 4.13 (a through e). The sub-surface of worn specimen of pure Cu has been observed to exhibit a small affected dark region underneath the worn area in Fig. 4.13 (a), whereas the sub-surface corresponding to composite CA reveals

plastic deformation accompanied by surface cracks, which appear to extend to the subsurface region of wear scar as seen in Fig. 4.13 (b). However, a number of cracks could also be observed even on the unaffected sub-surface area pointing towards the existence of inherent cracks within the material. The subsurface of CAM composite exhibits very small deformed region compared to that of pure Cu and CA composite, as shown in Fig.4.13 (c). The subsurface of CAMB composite shown in Fig. 4.13 (d) suggests the formation of layer over the worn surface as indicated by the ellipse on the micrograph. In order to further explore the nature of this layer, Fig. 4.13 (e) shows a magnified view of the layer which clearly reveals the formation of mechanically mixed layer. The worn surface of pure Cu enriched with plastically deformed regions has been observed to exhibit no signature of crack propagation towards the subsurface, whereas very rough and cracked features could be seen at the sub-surface of composite CA. These cracks are extended to underneath area and degree of plastically deformed region is noted to be higher than that of pure Cu. The CAM composite has been found to undergo minimum plastic deformation region amongst all materials studied in the present investigation.

Figures 4.14 (a through d) show the topographic images of worn tracks of pure Cu and Cu-based hybrid composites, examined under Atomic Force Microscope (AFM). The worn surface of pure Cu exhibits a peak-to-peak roughness ~ 1100 nm with peaks being round in nature as seen from Fig. 4.14 (a), whereas topographic features of worn surface of CA composite reveals a relatively higher peak-to-peak roughness (1300 nm) with very sharp spikes/peaks distributed over the whole area. The peak-to-peak roughness has been found to be around 1100 nm for composite CAM with peaks being less sharp and evenly distributed over the worn area as suggested by the image shown as in the Fig. 4.14 (c). However, the topography of the worn surface of composite CAMB

displays distant peaks with a peak-to-peak roughness of 650 nm. The topographic features of pure Cu supported by curved and distant peaks indicate that pure Cu copper has suffered a mild abrasion during the wear test. However, the presence of very rough, sharp and dense peaks on the worn surface of composite CA suggests the possibility of occurrence of a severe abrasion during the wear test. Both CAM and CAMB composites appear to have undergone a relatively milder abrasive events as suggested by their respective topographic features presented in Figs. 4.14 (c) and 4.14 (d).

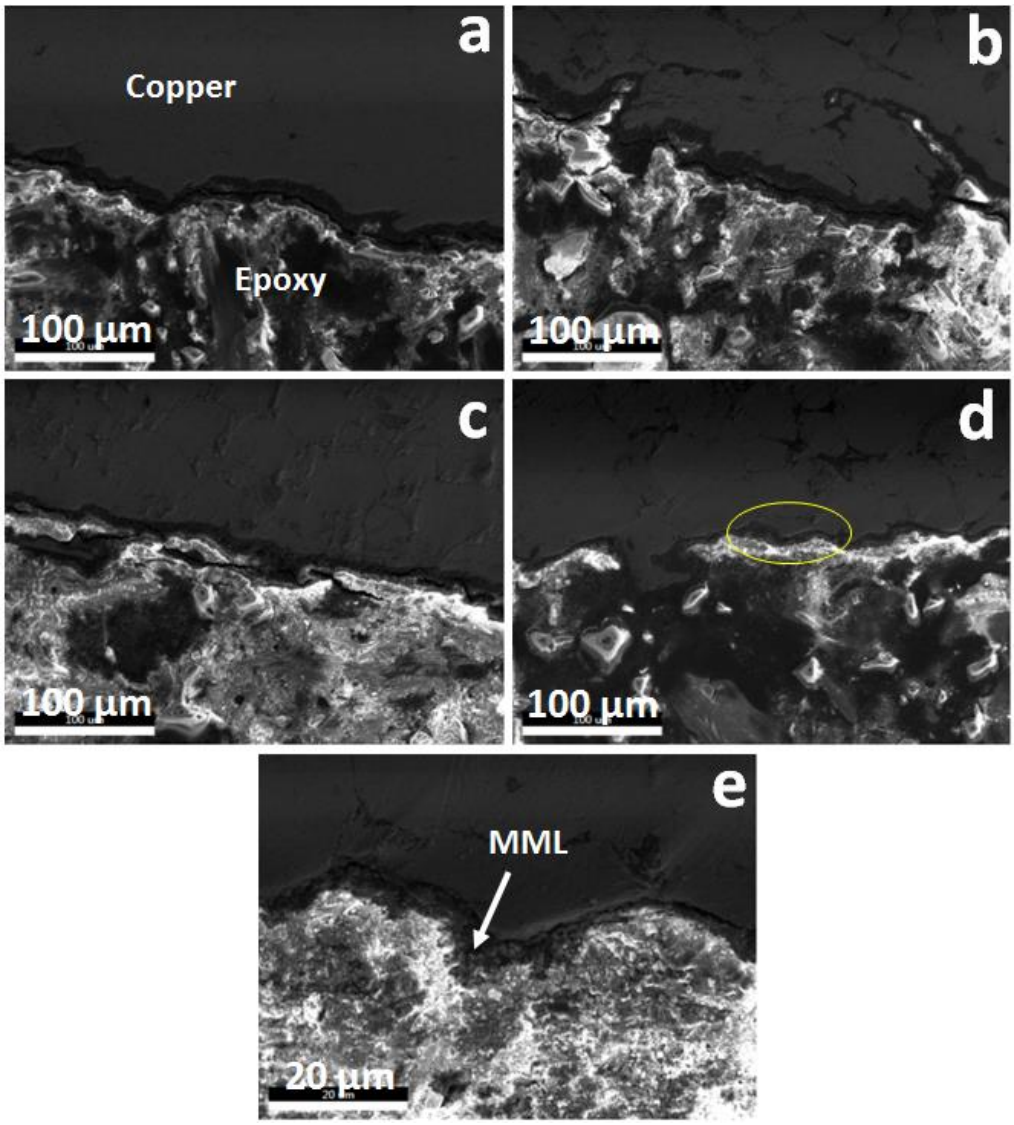

Fig. 4.13 Micrographs of worn sub-surfaces of (a) pure Cu and (b-d) Cu-based hybrid composites CA, CAM, and CAMB, respectively. (e) The magnified circular area of CAMB composite (d). Load: 8 N

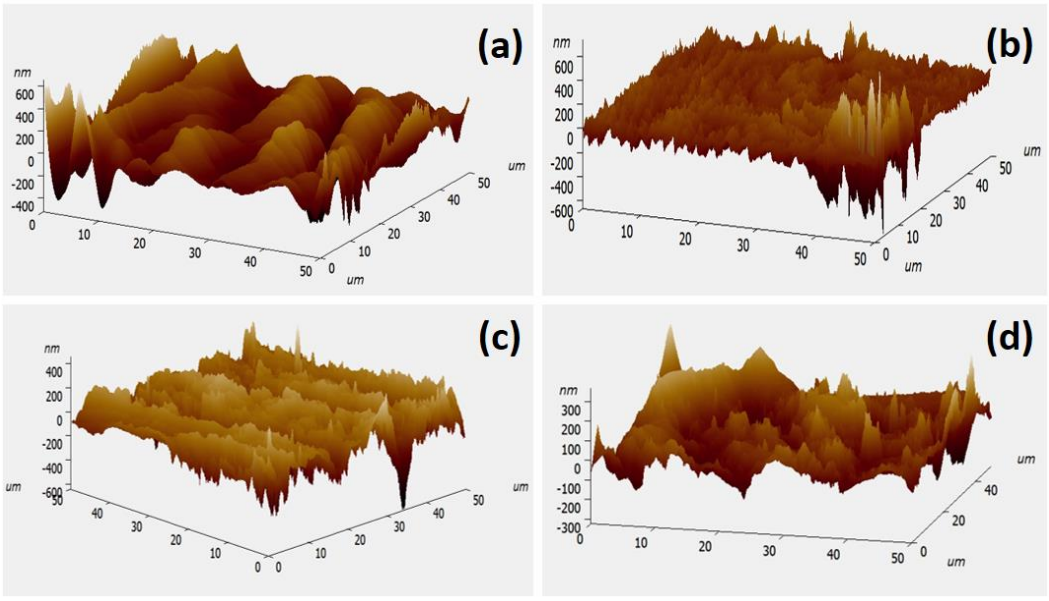

Fig. 4.14 Topographic images of worn surfaces of (a) pure Cu and (b-d) Cu-based hybrid composites CA, CAM, and CAMB, respectively, scanned by AFM. The EN 31 steel ball was used as counterface. Load: 8 N, sliding speed: 0.5 $m.s^{-1}$.

4.2 DISCUSSION

The microstructural features of the composites are shown with the help of scattered as well as backscattered mode of SEM in Fig. 4.2, while the distribution of the constituents is analyzed from elemental mapping shown in Fig 4.3. The microstructure of composite CA given in Fig. 4.2 (a) reveals the agglomeration of alumina particles along the grain boundaries, which lead to poor interfacial bonding between matrix and reinforcement phase. The agglomeration of alumina particles is confirmed by the elemental mapping shown in Fig. 4.3 (a). Figure 4.2 (b) shows the micrograph corresponding to the composite CAM, which unveils an almost uniformly dispersed MoS_2 phase throughout composite. however, number of pores are found to be less for CAM composite, which could be attributed to good wettability of MoS_2 as compared to alumina. The presence of MoS_2 particulates at the grain boundaries along with alumina is confirmed from the elemental mapping shown in Fig. 4.3 (b). From the microstructure of

composite CAMB shown in Fig. 4.2 (c) and elemental mapping in Fig. 4.3 (c), one may observe that *h*-BN not only obtain at the grain boundary positions but it can be seen inside the grains also, however, number of pores increases in CAMB composite, which ascribes to the poor sintering behavior of *h*-BN due to its inert nature.

The composites have shown a significantly higher hardness in comparison to pure copper, as evident from Table 4.1. The increase in hardness of CA composite compared to pure Cu may be attributed to a combination of plausible mechanisms of thermal mismatch and Orowan strengthening. A significant difference in thermal expansion coefficients Cu and alumina results in development of internal stresses leading to generation of dislocations which in turn, results in strain hardening and a consequent increase in hardness. The other contribution may come from Orowan strengthening mechanism wherein the alumina nano-particles offer hindrance to the movement dislocations and cause an increase in hardness. The hardness of composite containing Cu-Fe-Al_2O_3-MoS_2 i.e. CAM is observed to be the highest among all the materials. A marginal increase in hardness of CAM in comparison to CA (containing Fe and Al_2O_3) despite the addition relatively softer MoS_2 in comparison Al_2O_3 could be attributed to a comparatively better wettability between Cu-MoS_2 in comparison to Cu-Al_2O_3 which might have enhanced the bonding in CAM in comparison CA, which is further confirmed by the increase in relative density (Table 4.1) and more uniform dispersion of reinforcement as seen from Fig. 4.2 (b). The decrease in density and hardness of the composite CAMB could be attributed to the poor sintering behavior of *h*-BN, which is further supported by the voids and agglomeration of the particulates as observed in Figure 4.2 (c).

The effect of load on average coefficient of friction and wear rate has been observed on copper based composites containing Fe, Al_2O_3, MoS_2 and *h*-BN under

different loads of 2, 4, 6 and 8 N at fixed sliding speed 0.5 m. s^{-1} in Fig. 4.5 (a) and 4.6 (a), respectively. The average coefficient of friction and wear rate have been observed to increase with increase in load from 2 to 4 N for all the composites, this behavior may be explained with the help of worn surface micrographs shown in Figs. 4.7 and 4.8, respectively. Pure copper exhibits the value of average coefficient of friction as 0.58 and minimum wear rate among all composites under the load of 2 N, which may be ascribed to the mild adhesion as the wear mechanism, which is evident from the worn track shown in Fig. 4.7 (a). Whereas, the average coefficient of friction for composite CA has been observed to be marginally less than the value for pure copper tested under the load of 2 N, however the wear rate is observed to be higher than that of wear rate for pure copper, which may be attributed to adhesion driven delamination and oxidation as the operating wear mechanisms for the composite CA, as observed from the worn surface micrograph shown in Fig. 4.7 (b). A relatively lower coefficient of friction recorded for composite CA compared to pure copper, despite having high worn surface area and severe wear characteristics may be attributed to the release in energy in the form of material loss due to wear. The average coefficient of friction shown by composite CAM is minimum (~ 0.28) among all the composites at the load of 2 N as shown in Fig. 4.5 (a) and the a relatively lower wear rate in comparison to composite CA (Fig.4.6 a) may be attributed to the presence of compacted layer of wear debris on the worn surface shown in Fig. 4.7 (c) containing lubricating phase also as indicated by the selected area EDX (shown at lower right side of Fig. 4.7 c). The compacted layer helps in inhibiting the direct metal-metal contact between the specimen and the counterface whereas, the presence of lubricious phases provide the low shearing interface with a consequent reduction in coefficient of friction and wear. (Gautam et al., 2020). However, the wear rate of pure copper is slightly lower than that the wear rate of CAM composite at the load of 2N, which can be explained from the high worn surface area observed for composite CAM

compared to the worn track area corresponding to pure copper in Fig. 4.7 (c) and (a). The addition of *h*-BN in composite results in increase of average coefficient of friction nearly comparable to the coefficient of friction value of CA and highest wear rate among all the composites, as seen from Fig. 4.5 (a) and 4.6 (a), and the same may be attributed to the occurrence of plastic deformation and abrasion as seen in Fig. 4.7 (d). The white patches in Fig. 4.7 (d) represent the abraded region and the selected area EDX reveals that white patches contain high nitrogen, which indicates the pull out of *h*-BN particles and poor synergy of *h*-BN with MoS_2. An increase in coefficient of friction and wear rate is observed with increasing load from 2 to 4 N as seen from Fig. 4.5 (a) and 4.6 (a) may be explained with the help of worn surface micrographs of all the materials given in Fig. 4.8 (a through d). The transition of wear mechanism from mild adhesion to severe abrasive wear can be observed on increasing the load from 2 to 4 N for pure copper. The abrasion leads to digging by the hard asperities of the counterface into the relatively softer specimen leading to generation of wear debris which may act as third body after getting trapped between the sliding surfaces, if remains loose and results in an increase in coefficient of friction and wear rate. The increase in average coefficient of friction and the wear rate for composite CA with increasing load from 2 to 4 N as shown in Fig. 4.5 (a) and Fig. 4.6 (a) may explained on the basis of the SEM micrograph of the worn surface shown in Fig. 4.8 (b). The severity of delamination and oxidation is observed to increase with increase in load which may be judged from a comparison of Figs. 4.7 (b) and 4.8 (b) at 2 and 4 N loads, respectively, which may explain an increase in friction and wear for CA composite. The average coefficient of friction and the wear rate for composite CAM have been observed to increase as the load is increased from 2 to 4 N. It may be noted that the increase is minimum among all the composites at this particular load which may be attributed to the formation of compact layer over the worn surface as seen from Fig.4.8 (c). The formation of a compacted layer brings about a decrease in both the coefficient of

friction and wear rate only if the layer is intact and does not get detached from the surface. An increase in coefficient of coefficient and wear rate despite the presence of a compacted layer may be attributed to the detachment of the compact layer at some sites as visible in Fig. 4.8 (c). The composite CAMB exhibits increase in the value of average coefficient of friction from 0.56 to 0.77 on increasing the load from 2 to 4 N, which is highest among all the composites except for the pure copper and maximum wear rate is recorded for CAMB among the composites, at this particular load. This behavior can be explained with the help of worn surface micrograph shown in Fig. 4.8 (d), which reveals the increase in abrasion and plastic deformation with increase in load. The plastic deformation is associated with the mechanical work to deform the material plastically and contributes in coefficient of friction, while abrasion accounts for the direct asperity to asperity contact and results in increase in coefficient of friction and wear rate. The high wear rate of composite CAMB among all composites may be due to the pull out of *h*-BN particulates due its poor sintering characteristics because of which it is not able to integrate properly in the matrix as reported earlier by Tyagi et al. (2011). The variation of coefficient of friction with number of cycles, tested under the load of 8N shown in Fig 4.4, depicts the fluctuating trend. The maximum fluctuations can be observed for composite CA followed by CAM, pure copper and CAMB. The fluctuating trend accounts for the variation in contact when surface and counterface are evolving to develop a conformal contact. Whereas, the maximum average coefficient of friction has been recorded for CA followed by CAMB, CAM and pure copper, as shown in Fig. 4.5 (a). A sharp decrease in the value of average coefficient of friction (~0.32) and wear rate is observed for pure copper on increasing the load from 4 to 8 N, which is quiet an interesting result. Moreover, the value of the average coefficient of friction for Pure Copper has been observed to be less than the composites containing the solid lubricants, as observed from Fig. 4.5 (a). The frictional behavior under the load of 8 N, may be explained on the basis of (i) analysis for

worn surface, wear debris and subsurface morphology, (ii) XRD analysis for worn surfaces and (iii) AFM analysis for worn surfaces. The worn surface micrograph for pure copper demonstrates the presence of a smooth and compact layer with mild adhesion, as seen in Fig. 4.9 (a), the compact layer formation may be attributed to the enhanced frictional heating at relatively high loads which helps in compaction of the wear debris. This compacted layer inhibits the direct metal-metal contact and results in low coefficient of friction and wear rate as explained earlier. However, the mild adhesion has also been observed on worn track of steel ball counter face (Fig. 4.11 a), which may be attributed to the softening of junctions at the interface due to frictional heat and this might have also helped in reducing the friction. The AFM topographic micrograph corresponding to pure copper shown in Fig. 4.14 (a), explicitly shows the smooth and curvy profiles with distant and blunt peaks indicating the absence of abrasive wear, while subsurface micrograph shown in Fig. 4.13 (a) reveals the plastic deformation as one of the contribution factor for friction, which might have occurred under high load. However, a critical analysis of worn surface reveals that the low coefficient of friction for pure copper accounts for mild adhesion and plastic deformation under the load of 8 N. The average coefficient of friction (~0.8) and wear rate for composite CA is observed to increase with increase in load from 4 to 8 N, which is maximum among all the composites at this load, as seen from Fig. 4.5 (a) and 4.6 (a). The increase in average coefficient of friction and wear rate with increasing load may be attributed to transformation of wear mechanism from delamination and oxidation to three body abrasion, which is confirmed by the presence of loose wear debris on the worn surface of CA shown in Fig. 4.9 (b). X-ray diffraction of the worn track indicates that the loose particles over the worn surface contain CuO, which might have assisted three body abrasive wear (Fig. 4.10). One may also observe the formation of a lump over on the worn surface of counter face steel ball along with the presence of cracks and signs of delamination (Fig. 4.11 b), which may cause two body

abrasion. The combination of two and three body abrasion leads to large and irregular shaped chunk wear debris shown in Fig. 4.12 (a), which is the characteristics of severe wear and its scratchy and rough morphology further confirms the three body abrasive wear. The AFM micrograph reveals the closely packed sharp peaks representing the high number of asperities, which confirms the severe abrasive wear due to two and three body abrasion. The two and three body abrasion does not confine to the abrasive wear alone, yet these are also responsible for brittle fracture caused under the cyclic tribo-stress and fatigue wear as confirmed from the subsurface micrographs depicting the micro-cracks in Fig. 4.13 (b), which explains the reason for high coefficient of friction and high wear rate. The above discussion highlights that the coefficient of friction and wear rate for composite CA are associated with several wear mechanisms: abrasion, fatigue and delamination. The composite CAM exhibits the value of coefficient of friction as 0.2 for initial 1200 number of cycles whereas the coefficient of friction shoots around the value of 0.6 beyond that as shown in Fig. 4.4, while the average value is minimum among all the composites (~ 0.6) except pure copper (Fig. 4.5 a) and does not show any significant increase with increase in load from 4 to 8 N. Whereas, wear rate is observed to be the minimum among all the composites and marginally decreases with increase in load from 4 to 8 N. The frictional and wear behavior of CAM composite may be attributed to the formation of compacted layer, formed by the compaction of wear debris for initial sliding contact and its detachment after few cycles, as shown in Fig. 4.9 (c). The detachment of compacted layer may be attributed to the occurrence of the tribo-chemical transformation of MoS_2 into Mo_2S_3 (Furlan et al., 2018), as confirmed from the XRD shown in Fig.4.10. However, the compound Mo_2S_3 is hard in nature which might have contributed in lowering the wear rate, but not in friction reduction as it does not possess effective lubricating characteristics. The worn surface of counter face steel ball slid against CAM exhibits the transfer layer formation as seen from Fig. 4.11 (c) which lowers the friction

and wear by inhibiting the direct metal to metal contact. The subsurface micrograph shown in Fig. 4.13 (c) suggest the moderate amount of plastic deformation which might have also contributed towards the reduction in coefficient of friction. The topographic morphology as observed under AFM exhibits sharp, dense, and high roughness peaks which also represents the asperities at the worn surface, as shown in Fig. 4.14 (c). The formation of asperities on the worn surface has been ascribed to the detachment of compact layer, which results in high coefficient of friction due to direct asperity to asperity contact at the sites of compact layer detachment. The decrease in wear rate of CAM composite with increase in load from 4 to 8 N may be ascribed to the better compaction of wear debris, which is further confirmed by comparing the worn surface area shown in Fig. 4.8 (c) and 4.9 (c). The average coefficient of friction and wear rate for composite CAMB have been observed to decrease with increase in load from 4 to 8 N, while the coefficient of friction is comparable to the friction coefficient of CA composite, as shown in Fig. 4.5 (a). This frictional and wear behavior may be explained with the help of worn surface micrograph shown in Fig. 4.9 (d), which shows the presence of a bright smeared layer over the worn surface consisting of *h*-BN particles due to pull out, as confirmed by the XRD analysis of worn surface in Fig. 4. 10. The worn surface of steel ball slid against CAMB exhibits a thin crescent-shaped patch over the surface along with sliding marks adjacent to crescent feature, which indicates mild abrasive wear with minor adhesion, while formation of crescent feature could be associated with low adhesion at the rear side of the contact area of the ball, as shown in Fig. 4.11 d. The fine and regular shaped wear debris are obtained for CAMB composite as compared to that of wear debris obtained for CA, which supports the low friction and low wear of CAMB compared to CA composite, however, wear debris may get trapped between the mating surface and result in increase in friction. The subsurface micrograph corresponding to the composite CAMB shown in Fig. 4.13 (d-e) confirms the accumulation of wear debris over

the worn surface, which reveals the negligibly low plastic deformation. However, the presence of a mechanically mixed layer (MML) can be explicitly seen in high magnification subsurface micrograph, which may inhibit the direct metal to metal contact and decrease the friction and wear. Despite the MML formation, the average coefficient of friction and wear rate is higher than that observed for pure copper and CAM composite, which indicates that effective compaction of worn particles could not take place as compared to pure copper and CAM which may be attributed to the pullout of *h*-BN particulates due to their poor integration with matrix and absence of any synergetic action between *h*-BN and MoS_2. Also, occurrence of abrasion is confirmed from the AFM topographic micrographs shown in Fig. 4.14 (d), which shows distant peaks and low roughness.

Based on the results and discussion presented above it can be inferred that both coefficient of friction and wear increase with increasing load from 2 to 4 N for pure copper and composites containing Cu-Fe-Al_2O_3, Cu-Fe-Al_2O_3-MoS_2 and Cu-Fe-Al_2O_3-MoS_2-*h*-BN, whereas a further increase in load to 8 N leads to minor changes in coefficient of friction in the composites. However, a significant reduction in coefficient of friction from (0.93 to 0.32) is found to occur for pure copper, which has been attributed to the formation of compact layer due to frictional heating. The wear rate also decreases for all the composites except Cu-Fe-Al_2O_3 with increasing load from 4 to 8 N which has been attributed to the formation of a well compacted layer wear debris at the sliding surface due to higher frictional heating at high load. This layer inhibits direct metal to metal contact and results in lowering of wear rate. An increase in wear rate for composite Cu-Fe-Al_2O_3 with increase in load from 4 to 8 N has been attributed to three body abrasion caused by the loose wear debri. Among all the composites CAM (Cu-Fe-Al_2O_3-MoS_2) exhibits lowest wear rate and moderate coefficient of friction under the conditions

used in the present study. The results also reflect the absence of any synergetic action between *h*-BN and MoS_2 in providing enhancing the regime of lubrication. Hence, further studies have been conducted on Copper based composites containing reduced graphene oxide (rGO) and MoS_2 as lubricants and the results on their tribological behavior have been present in chapter 5 and 6.